



RESEARCH ARTICLE

10.1002/2016JC012545

Observations of waves and currents during barrier island inundation

A. Engelstad¹ , B.G. Ruessink¹ , D. Wesselman¹, P. Hoekstra¹ , A. Oost^{1,2}, and M. van der Vegt¹ ¹Faculty of Geosciences, Department of Physical Geography, Utrecht University, Utrecht, The Netherlands, ²Deltares, Delft, The Netherlands

Key Points:

- Elevated water levels in the Wadden Sea during storms can drive offshore flow during inundation
- Waves are coming from both sides of the barrier island and lose their energy primarily by wave breaking
- Infragravity waves crossing the submerged barrier island were onshore progressive, displayed a bore-like shape and were breaking

Correspondence to:

A. Engelstad,
A. C. Engelstad@uu.nl

Citation:

Engelstad, A., B. G. Ruessink, D. Wesselman, P. Hoekstra, A. Oost, and M. van der Vegt (2017), Observations of waves and currents during barrier island inundation, *J. Geophys. Res. Oceans*, 122, 3152–3169, doi:10.1002/2016JC012545.

Received 11 NOV 2016

Accepted 14 MAR 2017

Accepted article online 17 MAR 2017

Published online 13 APR 2017

Abstract Overwash and inundation on barrier islands can transport sediment onshore, leading to vertical accretion. These processes could ensure barrier island growth in times of sea-level rise, but wave and current fields during overwash and inundation are not well understood. Field data of water levels, waves, and currents were collected on a barrier island in the Netherlands to investigate the hydrodynamics during island inundation. Observations show that even in shallow water depths (<0.5 m) wave energy was not completely dissipated as waves propagated from the North Sea onshore. Additionally, locally generated wind waves entered the field area from the Wadden Sea and propagated offshore. Infragravity waves were an important part of the wave field, particularly onshore of the beach crest. They were observed to be onshore progressive and displayed a bore-like shape when water depths were shallow. Wave breaking was the dominant dissipation mechanism for high-frequency waves as well as for infragravity waves, which is in agreement with prior research on infragravity wave energy dissipation on mild sloping (closed-boundary) beaches. A large-scale offshore directed water-level gradient between the Wadden Sea and the North Sea side, caused by elevated water levels in the Wadden Sea during the storms, frequently drove an offshore flow if it was large enough to exceed the cross-shore gradient due to wave setup. In addition, elevated water levels in the Wadden Sea decreased current velocities due to a decrease in water-level gradients. This study highlights the influence of back-barrier processes on the hydrodynamics during inundation.

1. Introduction

The accretion of sediment on barrier islands is essential for increasing the stability of barrier islands in times of sea-level rise. Overwash on barrier islands and island inundation could increase the resilience of barrier islands [Oost *et al.*, 2012] due to the associated onshore sediment transport [Leatherman, 1976; Sallenger, 2000]. During overwash, water carrying suspended sediments overtops the beach crest or dune crest without directly returning to the sea [Donnelly *et al.*, 2006]. Once the beach and foredunes are continuously submerged, this process is defined as inundation [Sallenger, 2000]. Overwash and inundation typically occur during extreme events such as storms and hurricanes when water levels are elevated by storm surges and wave setup. These processes can cause large-scale coastal changes, such as the breaching of barrier islands and island instabilities [Donnelly *et al.*, 2006; Safak *et al.*, 2016] and the landward transition of islands (roll-over), but it can also lead to vertical growth. The impact of overwash and inundation is particularly noticeable for low-lying, narrow, microtidal barriers in the US where overwash and inundation events are driven by hurricanes [Fisher *et al.*, 1974; Leatherman, 1976; FitzGerald and Pendleton, 2002; Donnelly *et al.*, 2006]. However, overwash and inundation also occur on barrier islands and spits in Europe under mesotidal settings with extratropical storms such as in Portugal, Denmark, Germany, and the Netherlands [Matias *et al.*, 2010; Christiansen *et al.*, 2004; Nielsen and Nielsen, 2006; Hoekstra *et al.*, 2009; Oost *et al.*, 2012; Van der Vegt and Hoekstra, 2012]. In mesotidal, mixed energy systems, overwash and inundation can result in net vertical growth of the islands, particularly on the broader and higher barrier islands in the North Sea [Nielsen and Nielsen, 2006; Christiansen *et al.*, 2004].

Because it is inherently difficult to measure wave dynamics and flow dynamics during storm conditions, not much is known about the hydrodynamic processes. Most of the conducted studies focused on morphological changes before and after storms [Morton and Sallenger, 2003; Nielsen and Nielsen, 2006; Matias *et al.*,

© 2017. The Authors.

This is an open access article under the terms of the Creative Commons Attribution-NonCommercial-NoDerivs License, which permits use and distribution in any medium, provided the original work is properly cited, the use is non-commercial and no modifications or adaptations are made.

2008], laboratory work [Edge et al., 2007; Matias et al., 2013], and numerical modeling [Van Dongeren and Van Ormondt, 2007; McCall et al., 2010, 2011]. Some studies include onsite hydrodynamic measurements [Fisher et al., 1974; Leatherman, 1976; Holland et al., 1991; Hoekstra et al., 2009; Matias et al., 2010; Van der Vegt and Hoekstra, 2012; Sherwood et al., 2014]. Generally, there is not much detailed field data on the hydrodynamic conditions during overwash and inundation events. Wave processes are relatively well studied and understood on a closed surfzone-beach-dune system (without overwash or inundation). However, basic processes such as current magnitudes and directions and wave transformation are less well analyzed and understood during inundation. For example, low-frequency ($\sim 0.005\text{--}0.05$ Hz) infragravity wave reflection and return flows, which can be important on closed beaches [Guza and Thornton, 1985; Herbers et al., 1995; Ruessink et al., 1998; Janssen et al., 2003], may be reduced or absent during overwash and inundation. This could effectively alter the cross-shore and alongshore wave and current dynamics over the inundated area compared to a closed beach. Of interest is also how the incident wave field transforms over long stretches of shallow water depths on gentle slopes. Video observations by Hoekstra et al. [2009] showed that while the incident wave field was composed of high-frequency ($\sim 0.05\text{--}1$ Hz) and infragravity waves during an overwash event, the high-frequency waves were dissipated as they propagated across the very wide beach of the barrier island. The observed erosion of the dunes, therefore, was primarily caused by low-frequency waves. Additionally, during the inundation of barrier islands both waves and water are able to enter from the sea as well as from the back-basin area. Water levels might be elevated in the backbarrier basin, for example, due to winds, tidal phase lags, or wave-driven water fluxes into the back-barrier area [Sherwood et al., 2014]. Observations [FitzGerald and Pendleton, 2002; Hoekstra et al., 2009; Sherwood et al., 2014] and modeling results [Van Dongeren and Van Ormondt, 2007; Sherwood et al., 2014] suggest that higher water levels on the basin side create a hydraulic gradient that is able to drive a flow from the basin to the sea side, initially preventing the flow from the sea to reach the back barrier [Van Dongeren and Van Ormondt, 2007]. The hydraulic gradient can then potentially lead to sediment deposition on the seaward side of a barrier island [Sherwood et al., 2014].

In the Netherlands, most barrier islands are heavily guarded by natural dunes and sand drift dikes (sand blown artificial dunes) to protect the islands against storms from the ocean side (North Sea) and the back-barrier basin (Wadden Sea), effectively cutting off any sediment supplies landward of the dunes. At present, the re-opening of dunes and dikes is considered for uninhabited areas. A new paradigm in coastal zone management includes a more flexible and dynamic behavior of the coast by facilitating natural hydrodynamics and geo-ecological processes wherever safely possible to enhance coastal resilience. However, to evaluate the feasibility and effectiveness of restoring such natural processes, the hydrodynamics during overwash and inundation need to be better understood. The objectives of the present work are to examine the transformation of infragravity and high-frequency waves as they propagate across the inundated part of a barrier island, and to investigate the dominant dissipation mechanisms. Further, the effects of water levels, wave forcing and wind forcing on the cross-shore flow velocities are investigated, and the importance of back-barrier processes is considered. This is done by analyzing a hydrodynamic data set, collected in the course of a 3 month field campaign on the Dutch island of Schiermonnikoog. The field site, the instrumentation, and the boundary conditions are described in section 2. In section 3, the data processing and the methodology used to analyze the wave and flow fields are introduced. Section 4 presents the results on waves and currents. The limitations of a 1-D approach, the similarities of wave processes for open and closed-boundary systems, and the importance of the back-barrier basin are explored in section 5. Finally, conclusions are given in section 6.

2. Data Collection and Boundary Conditions

2.1. Field Site

Field data were collected on the eastern tip of the Dutch barrier island Schiermonnikoog (Figure 1) during a 3 month campaign from November 2014 until the end of January 2015. Schiermonnikoog is part of a barrier island chain fronting the coasts of the Netherlands and Germany (Figure 1). These barrier islands separate the North Sea from the Wadden Sea (the back-barrier basin). Schiermonnikoog is almost 18 km long, 3 km wide at its up-drift western end and about 1.5 km wide at its narrowest down-drift eastern end. The eastern end of the island is still growing and has, in fact, grown ~ 3 km toward the east since 1982 [Loeffler et al.,



Figure 1. Barrier islands fronting the coasts of the Netherland and Germany. The Wadden Sea encompasses a series of back-barrier basins between the islands and the coast. The field site (marked by the orange squares) was located on the eastern tip of the barrier island Schiermonnikoog.

2011]. The mean offshore significant wave height is 0.5–1 m in the summer (April to October) and 1–2 m in the winter (October to April), while significant wave heights during storms can reach 8–11 m during north-westerly winds [Oost *et al.*, 2012]. The system is mesotidal, mixed-energy, and tide-dominated, with a tidal range of ~ 1.5 –2.3 m. The tidal wave propagates toward the east. Storm surges can significantly increase water levels along the barrier islands and the coast, potentially leading to severe flooding of unprotected areas. The highest recorded setup of water levels during storm surges was ~ 3.5 –4 m [Hoekstra *et al.*, 2009; Oost *et al.*, 2012].

The field site is subaerial but free of vegetation and inundation only occurs during storms when water levels are elevated. The coastline is aligned $\sim -10^\circ$ with true East, and the area is approximately alongshore uniform for at least 1 km on both sides of the instrument transect. However, a tidal inlet channel is situated ~ 1.5 km to the east. The maximum height in the cross-shore profile is ~ 1.6 m above mean sea level (MSL) (Figure 2), allowing for a higher frequency of flooding than in other parts of the island. In addition, the area is open to flooding from the North Sea side as well as from the back-barrier basin.

2.2. Instrumentation

To measure water levels, flow velocities, and waves, instruments were placed roughly cross-shore (Figure 1) at 0.1–0.2 m above the bed. The instrument transect stretched across the island from the North Sea to the Wadden Sea over a distance of ~ 1.3 km (Figure 2). The instrument array consisted of three instrument frames, each equipped with an Acoustic Doppler Velocimeter (Nortek vector, cabled version), sampling pressure and velocity continuously at 16 Hz. An additional pressure sensor (Ocean Sensor System Wave Gauge, type OSSI-010-003C) was collocated to the Acoustic Doppler Velocimeter (ADV) at the Wadden Sea (labeled P9 in Figure 2), because of a potential drift in the ADV-pressure offset. In addition, nine stand-alone pressure sensors (also Ocean Sensor System Wave Gauge, type OSSI-010-003C) were placed along the instrument-transect (labeled P1–P8 and P10 in Figure 2). All stand-alone pressure sensors sampled

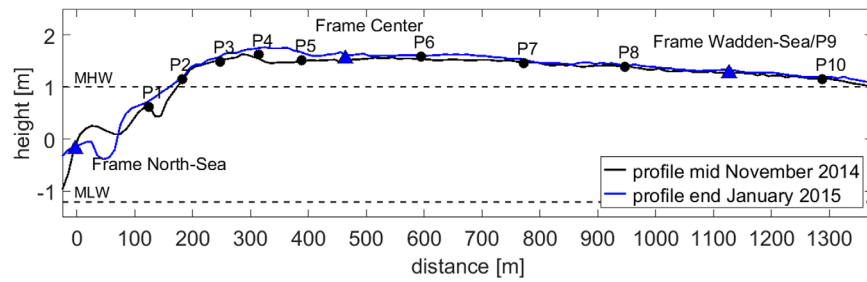


Figure 2. The cross-island profiles in mid-November 2014 (black curve) and at the end of January 2015 (blue curve) are shown with the North Sea to the left and the back-barrier area (Wadden Sea) to the right. Black dots mark the stand-alone Ocean Sensor System pressure sensors (P1–P10), while the blue triangles mark the instrument frames equipped with Nortek ADVs (pressure and currents). The dashed lines indicate mean high water (MHW) and mean low water (MLW) levels, respectively. The vertical datum is NAP (Dutch Ordnance Datum), where 0 m NAP corresponds to mean sea level.

continuously at 10 Hz with an accuracy of ~ 1 mbar. The transect profile and the height of the instrument locations were measured with a Real Time Kinematic Global Positioning System (RTK-GPS) with an accuracy of ~ 0.02 m in the horizontal and ~ 0.03 – 0.05 m in the vertical. The steepest slope of the profile is less than 1/100 (0.9/100 between P1 and P2), while the highest point of the profile (~ 1.6 m) was just north of P4. Grain sizes were analyzed from sediment samples collected at the center ADV (median grain size of 203 μm) and the Wadden Sea ADV (median grain size of 199 μm).

2.3. Boundary Conditions

Storm conditions with wind speeds ranging from 12 to 19 m/s and local wind directions from SW to NW (Table 1), measured at the offshore station Wierumergronden, caused water levels to increase (Table 1) and flood the field site. This led to 11 inundation events at the field site during the observational period. Inundation of the field site only took place during high tide, and the overwash regime was limited to a short period of time during the rising tide until the field site was inundated. Here, each flooding is treated as a single event although the field site might have been flooded multiple times during one storm. Only events during which all instruments were covered with water are considered. Inundation depths at P4 (Figure 3), the highest located instrument, were generally shallow (0.3–0.6 m), but reached 1.3 m during the largest event (flooding 9). Offshore significant wave heights, measured at station Schiermonnikoog Noord, ranged from 3.0 to 5.8 m (Table 1) with wave directions persistently from the NW. This is consistent with northerly wind directions offshore (not shown). Significant wave periods ($T_{1/3}$) varied between 8 and 12 s (Table 1). Water levels in the North Sea and in the Wadden Sea were measured by the tidal-stations Huibergat and Schiermonnikoog, respectively (Table 1).

Table 1. Boundary Conditions for All Observed Floodings^a

Flooding #	Date	Wind Speed (m/s)	Wind Direction (°)	Wave Hs (m)	Wave T (s)	Wave θ (°)	Water Level N. Sea (m)	Water Level W. Sea (m)
1	11 Dec 2014	13.86	243	4.08	10.6	298	1.98	2.05
2	11 Dec 2014	16.73	268	3.78	9.7	293	1.75	1.85
3	12 Dec 2014	12.56	246	4.02	10.0	297	1.75	1.85
4	20 Dec 2014	19.16	260	4.65	10.0	300	1.96	2.03
5	20 Dec 2014	15.15	308	4.97	11.0	319	1.74	1.98
6	02 Jan 2015	17.07	280	4.83	10.5	305	2.03	2.18
7	10 Jan 2015	16.70	243	3.13	9.9	303	1.91	1.95
8	10 Jan 2015	18.90	282	2.96	7.9	284	1.87	1.74
9	11 Jan 2015	17.95	269	5.88	12.1	312	2.65	2.87
10	11 Jan 2015	19.46	284	5.67	11.4	316	1.81	2.05
11	29 Jan 2015	16.24	251	4.38	10.4	300	2.08	2.17

^aIf dates are listed twice, two inundation events occurred on the same day and were separated by a low tide. Wind speeds and directions as well as significant wave heights (Hs) and periods (T), measured by an offshore meteorological station (Wierumergronden) and a wave buoy (Schiermonnikoog Noord), were averaged over 1 h at high tide. In addition, the water levels in the North (N) Sea (measured at Huibergat) and Wadden (W) Sea (measured at Schiermonnikoog station) are given, which were also averaged over 1 h at high tide.

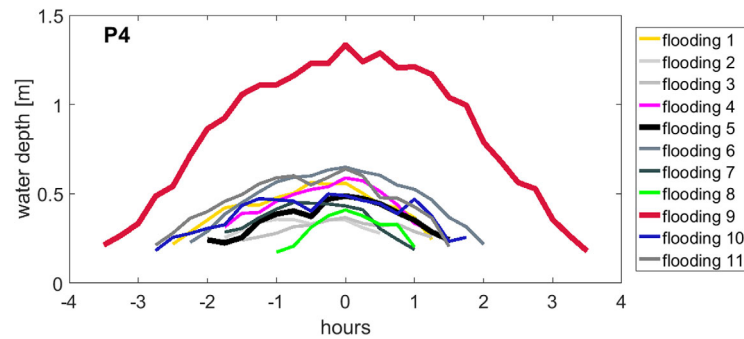


Figure 3. All inundation events are shown for the instrument closest to the crest (P4). The time on the x axis is set relative to high tide (0 h). The events marked by the thick black line (flooding 5) and the thick red line (flooding 9) will be used in the analysis and the discussion as examples for shallow and deep floodings, respectively.

free surface elevation using linear wave theory. The free surface elevation was then lowpass (0.005–0.05 Hz) and highpass (0.05–1 Hz) filtered, after which wave heights were calculated as four times the standard deviations of the filtered surface elevations. Additionally, the velocity data were objected to further quality controls following the guidelines by *Elgar et al.* [2005] and *Mori et al.* [2007]. If more than 10% of the record did not pass the quality control, the block was rejected, otherwise the data were interpolated. Since velocities were only available for a single height, the Karman-Prandtl boundary equation

$$U(z) = \frac{U_{*c}}{K} \ln \frac{z}{z_0} \quad (1)$$

was used to estimate the vertical current profile. Here U_{*c} is the current related shear velocity, K is the Van Karman constant (0.41), z is the height of the instrument above the bottom, and z_0 is the roughness length calculated from the median grain diameter. For this, U_{*c} was found from the single point measurements and in turn was used to estimate the velocities at 20 locations between the bed and the surface. Finally, the estimated velocities were averaged. Cross-shore and alongshore velocities account for the island angle.

Velocity data from the ADV on the North Sea side were not used, because the instrument was intermittently buried by sand, as was the first stand-alone pressure sensor (P1) on the North Sea side. Burial depths for this ADV pressure sensor and for P1 were visually estimated from the raw data during times when the instruments were not inundated and measured only air pressure and pore pressure. To account for instrument burial in calculations of the sea surface elevation, the correction factor of *Raubenheimer et al.* [1998] was used. Because P1 was intermittently buried, the water-level gradient between the North Sea and the Wadden Sea was calculated between P2 and P10, although using P1 and P10 gave similar results. Generally, water-level gradients were calculated by finite differencing over adjacent pressure sensors as

$$\frac{\delta \zeta}{dx} = \frac{\zeta(P_{n+1}) - \zeta(P_n)}{L} \quad (2)$$

where ζ is the water level at each instrument, which is the sum of averaged water depths and heights of the instrument location (with respect to MSL), and L is the distance between adjacent instruments. n indicates an instrument closer to the North Sea side whereas $n + 1$ indicates an instrument closer to the Wadden Sea side. For all instruments, the distance to the bed was measured at the beginning and the end of the campaign. The difference between these measurements was linearly interpolated. The largest bed level changes were observed in the zone between the mean high water (MHW) and mean low water level (MLW) and directly onshore of the crest (Figure 2).

3.2. Wave Transformation

To investigate the transformation of infragravity (0.005–0.05 Hz) and high-frequency (0.05–1 Hz) waves as they propagate across the field site, spectral estimates were obtained for one representative shallow flooding (flooding 5) and the deepest flooding (flooding 9). These examples will be used throughout this publication to highlight the influence (or lack thereof) of different inundation depths on wave and current dynamics. Assuming water levels to be approximately stationary around high tide, variance densities were

3. Data Analysis

3.1. Initial Data Analysis

Pressure and current velocities were processed in 15 min blocks for time series of water levels, wave heights, and cross-shore velocities. Clock-offsets within the stand-alone pressure sensors were linearly interpolated. Data were rejected when pressure sensor coverage was less than 0.04 m to avoid intermittent exposure to air. Pressure data were corrected for air pressure and converted to

estimated with Welch’s method using 1 h records of sea surface elevations, block lengths of 10 and 5 min overlap, resulting in 36 degrees of freedom. Further, the energy flux F was calculated as

$$F = \rho g E c_g \cos \theta \tag{3}$$

where ρ is the water density, g is the gravitational acceleration, E is the variance density, and c_g is the group speed in the shallow water approximation \sqrt{gh} , where h is the water depth. Waves are considered to be normally incident to the shoreline so that the mean angle of incidence, θ , is assumed to be 0° . Further, the cross-shore energy flux gradient, $\frac{dF}{dx}$, was estimated through finite differencing over adjacent stations and \bar{F} is the energy flux averaged between adjacent stations. To investigate energy losses (and gains) for high-frequency and low-frequency waves and to relate them to local aspects such as bottom slope and inundation depth without the dependency on the energy in the wave field, the normalized energy flux gradient, or growth rate, κ was used

$$\kappa = \frac{dF}{dx} \frac{1}{\bar{F}} \tag{4}$$

for which F was calculated in the low-frequency (0005–0.05 Hz) and high-frequency (0.05–1 Hz) bands.

To gain a better understanding of the dissipation mechanisms, the energy balance equation was considered as

$$\frac{dF}{dx} = S_{dis} \tag{5}$$

where S_{dis} is the dissipation term. While nonlinear energy transfers might be important [e.g., *De Bakker et al.*, 2016], they are ignored for the purpose of this study, as is the generation by wind. Dissipation contains dissipation by wave breaking (D_{br}) and by bottom friction (D_{bfr}) so that

$$S_{dis} = D_{br} + D_{bfr} \tag{6}$$

Wave breaking was estimated following *Thornton and Guza* [1983]

$$D_{br} = \frac{3\sqrt{\pi}}{16} \rho g \bar{f} \frac{B^3}{\gamma^4 h^5} H_{rms}^7 \tag{7}$$

where H_{rms} is the root-mean squared wave height and \bar{f} is the mean frequency. B is a breaker coefficient of $O(1)$ which accounts for different breaker types. The free model parameter γ is given by *Ruessink et al.* [2003] as

$$\gamma = 0.29 + 0.76 * kh \tag{8}$$

where k is the wavenumber. The mean frequency (\bar{f}), γ , and H_{rms}^7 were calculated in the high-frequency and low-frequency limits. Dissipation due to bottom friction [*Thornton and Guza*, 1983], calculated also in the above-mentioned frequency limits, was estimated as

$$D_{bfr} = \rho c_f \frac{1}{16\sqrt{\pi}} \left(\frac{2\pi\bar{f}H_{rms}}{\sinh(kh)} \right)^3 \tag{9}$$

where the bed friction coefficient c_f was calculated as [*Zijlema et al.*, 2011]

$$c_f = \frac{n^2 g}{h^3} \tag{10}$$

with the Manning’s roughness coefficient n set to 0.0225 [*Grunnet et al.*, 2004].

The onshore propagation of infragravity waves was investigated by establishing the cross-correlations between consecutive instruments after lowpass filtering the time series of sea surface elevations.

3.3. Momentum Balance

The cross-shore momentum balance was used to investigate how water levels, wave forcing and wind forcing effect flow velocities. The cross-shore momentum balance is considered over 1 h at high tide as:

$$h \frac{du}{dt} + hu \frac{du}{dx} = -gh \frac{\delta \zeta}{\delta x} - \frac{1}{\rho} \left(\frac{\partial S_{xx}}{\partial x} + \tau_{bot,x} - \tau_{wind,x} \right) \quad (11)$$

The terms from left to right are flow acceleration and advection, pressure gradient, wave force, bottom friction, and wind stress. Since velocities were only available for two locations, velocities from the center ADV and the Wadden Sea ADV were interpolated and extrapolated to P5–P10 so that flow acceleration, advection, and bottom friction could be estimated for these locations (they are not available for P1–P4). For the flow acceleration, $h \frac{du}{dt}$, the time step was an hour, and $\frac{du}{dx}$ was calculated as the difference in flow velocity between adjacent instruments, divided by the distance between these instruments. The water-level gradient $\frac{\delta \zeta}{\delta x}$ was estimated as the difference in the mean water level between adjacent instruments, again divided by the distance between these instruments. Here the water-level gradient is both the result of the local radiation stress, as well as the large scale difference in water levels between the North and Wadden Sea. The cross-shore component of the radiation stress was calculated in the shallow water approximation as [Longuet-Higgins and Stewart, 1964]

$$S_{xx} = 3/2E \quad (12)$$

where E is the variance density integrated over the frequency range 0.005–1 Hz. The bed shear stress can be approximated as [Ruessink et al., 2001]

$$\tau_{bot,x} = c_f \rho u \sqrt{(1.16u_{rms})^2 + u^2 + v^2} \quad (13)$$

where c_f is defined as in equation (10) and u and v are the depth-averaged mean cross-shore and along-shore velocities, respectively. Finally, the cross-shore component of the wind shear stress was calculated from

$$\tau_{wind} = \rho_{air} C_d U_{10}^2 \quad (14)$$

where ρ_{air} is the density of air, U_{10} is the wind speed at 10 m height obtained from the Wierumergronden meteorological station (averaged over an hour), and C_d is the wind drag coefficient calculated as 1.2875×10^{-3} for $U_{10} < 7.5$ m/s [Wamdi Group, 1988] and $(0.8 + 0.065U_{10}) \times 10^{-3}$ for $U_{10} \geq 7.5$ m/s [Wu, 1982].

Calculations of the cross-shore velocity u were done by substituting (13) into (11) and solving for u . Since the results give two possible solutions (positive and negative), the solution closest to the observation was chosen.

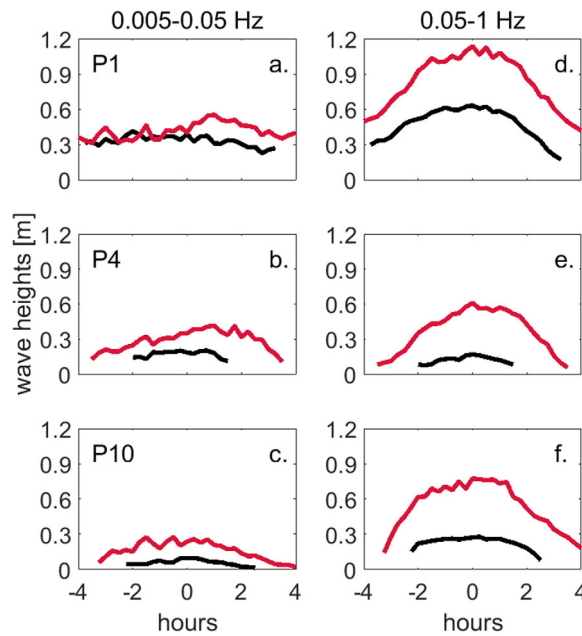


Figure 4. (a–c) Low-frequency and (d–f) high-frequency wave heights at the (a and d) North Sea side, (b and e) the crest, and (c and f) the Wadden Sea side. The red curve shows the deep flooding while the black curve shows the shallow flooding. Note that vertical scales are different for low and high frequencies. The time on the x axis is set relative to high tide (0 h).

4. Results

4.1. Waves

Time series of infragravity and high-frequency wave heights (Figure 4) were explored for the shallow and the deep flooding at the North Sea side (P1), the crest (P4), and the Wadden Sea side (P10). Sea-swell wave heights ranged from 0.6 to 1.2 m during high tide at the North Sea side (Figure 4a), and were significantly smaller at the crest (~0.15–0.6 m at P4) (Figure 4b) and at the Wadden Sea (~0.25–0.75 m at P10) (Figure 4c). Since waves were considerably higher offshore (5 and 5.9 m for the shallow and the deep flooding, respectively; Table 1), it can be assumed that most wave breaking already occurred further seaward of the field site.

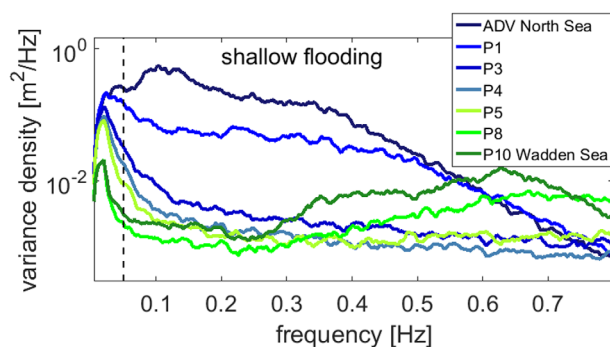


Figure 5. Variance densities for the shallow flooding. Results for the deep flooding are similar, but without the increase for frequencies >0.5 Hz. The dashed black line shows the cut-off between infragravity (0.005–0.05 Hz) and high-frequency (0.05–1 Hz) waves.

are only results for the shallow flooding, since results were similar for the deep flooding. Wave energy around the spectral peak (~0.1 Hz), indicating waves from the North Sea (Figure 5), dissipated as waves propagated toward the center and was lowest at P5. On the other hand, wave energy in the frequency band ~0.2–0.5 Hz increased between P5 and P10. Spectral directions indicate that waves in this frequency-range were actually coming from the South (not shown) during the shallow flooding. During the deep flooding, the velocity range of both ADVs was exceeded, and while unwrapping the data worked well for averages of 15 minutes, the data could not be recovered for reliable spectral directions for this case. The southerly direction suggests that these waves were locally generated in the Wadden Sea and propagated toward the center of the transect. This notion is supported by the wave spectrum from a directional wave rider buoy in the Wadden Sea at Pieterburenwad (to the southeast of Schiermonnikoog) where spectral peaks ranged between 0.25 and 0.5 Hz for almost all flooding events (not shown). During the shallow flooding, a strong increase in spectral densities is found for frequencies >0.5 Hz between P5 and P10 (Figure 5). For this frequency-range, winds from the NW with speeds of 15 m/s and wave directions from the NW suggest wind wave growth. This growth was absent during the deep flooding since the wind direction was normal (W) to the transect. Infragravity wave heights ranged from 0.3 to 0.6 m at the North Sea side and ~0–0.3 m at the Wadden Sea side (Figures 4d and 4e) at high tide, and appeared to be depth-modulated by tidal variations (Figures 4d–4f) like the high-frequency waves (Figures 4a–4c). Depth modulation of infragravity

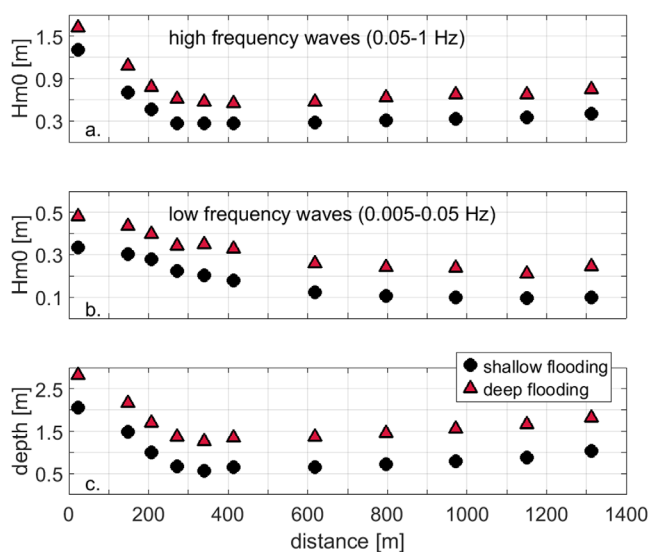


Figure 6. Significant wave heights for (a) high and (b) low frequencies compared to inundation depths (c) for the shallow (black dots) and the deep flooding (red triangles) averaged over 1 h at high tide. The North Sea is to the left of the graph and the Wadden Sea is to the right.

Interestingly, high-frequency wave heights were higher at the Wadden Sea side compared to the crest, which is especially notable during the deep flooding (thick red line in Figure 4) when wave heights were about 0.15 m higher at the Wadden Sea. This was unexpected, since waves were assumed to enter the field site from the North Sea, and substantial increases in wave height due to local wind forcing were thought to be negligible because of the oftentimes westerly wind direction (Table 1) and the relatively short fetch.

Spectral densities were used to evaluate the increase in wave heights. Shown here

waves was also noticed in observations on a fringing reef [Pomeroy *et al.*, 2012] and in model results [Van Dongeren *et al.*, 2013]. However, infragravity wave heights decreased until about P6 (Figure 6b) and then stayed approximately constant. This differs for the sea-swell waves which decreased rapidly with decreasing depths as they propagated onshore, which is consistent with depth-limited breaking (compare Figures 6a and 6c). Due to the slower decay in wave heights, infragravity waves became increasingly important at the center of the transect. Here, they were about equal in height to the high-frequency waves (Figures 4b and 4e), particularly during shallow events.

Correlation coefficients for infragravity waves at consecutive instruments, with average values of 0.9 at the North

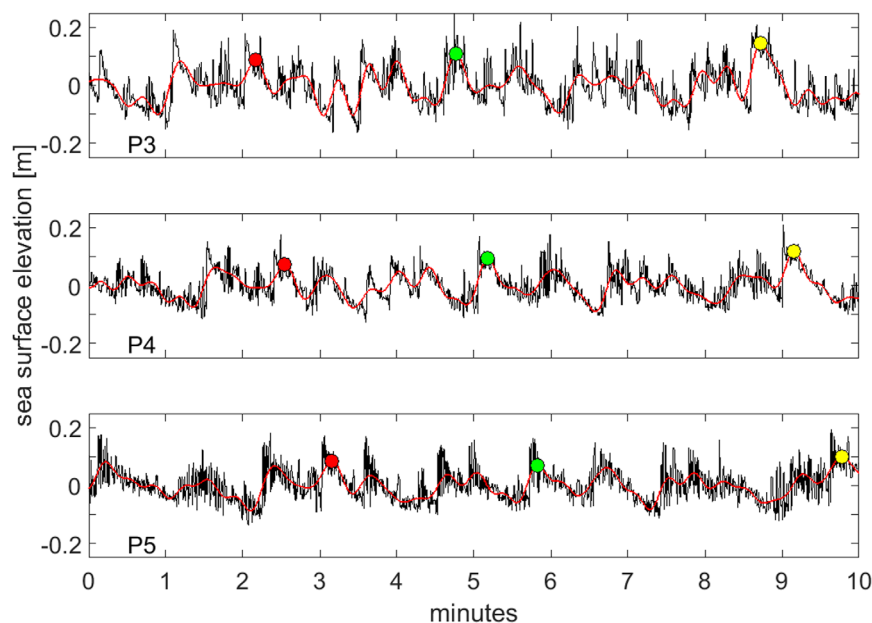


Figure 7. Time series of sea surface elevations (black curves) and low-pass filtered (0.005–0.05 Hz) infragravity waves (red curves) at stations P3–P5 (upper to lower plot) over 10 min at high tide during the shallow flooding. The red, green, and yellow dots are tracing single bores from instrument to instrument and are further discussed in the text.

Sea side, 0.8 right after the crest, and 0.3 at the Wadden Sea side, suggest that these waves were onshore progressive and unidirectional. The correlation was best close to the North Sea and decreased toward the Wadden Sea, coinciding with the decrease in wave heights. In shallow water depths, infragravity waves showed a bore-like shape (Figure 7) onshore of the crest up to \sim P6, suggesting that even after the crest part of the energy losses were caused by wave breaking. Tracking individual infragravity waves (see the colored dots in Figure 7) between P3 and P5 supports the notion of the onshore progressive nature of the waves. Using the time lag of the marked waves from P3 to P4 and from P4 to P5 and dividing it by the distance between the instruments (resulting in 2.96, 2.72, and 2.62 m/s between P3 and P4 and 2.02, 1.91, and 1.98 m/s between P4 and P5) gives a fairly good agreement with the calculated propagation speed (2.18 m/s between P3 and P4 and 2.17 m/s between P4 and P5) in the shallow water approximation \sqrt{gh} .

In the following, we explore the dissimilarity in energy losses for infragravity and high-frequency waves seen above in more detail, and aim to relate them to local aspects such as bottom slope and inundation depths. For this, growth rates were used (equation (4)) which are described below as P1–P2 for the growth rates between P1 and P2 up to P9–P10 for calculations between P9 and P10. Generally, negative growth rates indicate dissipation while positive growth rates indicate an increase in wave energy. However, due to the assumption that waves propagate onshore, the positive growth in the frequency range \sim 0.25–0.5 Hz from approximately P6–P7 to the Wadden Sea represents, in fact, dissipation of wave energy from the Wadden Sea, since waves in this frequency range propagated offshore.

Wave energy dissipation of high-frequency waves was strongest on the North Sea side (Figure 8) along the steepest parts of the slope (P1–P2 and P2–P3), indicative of depth-limited wave breaking [Herbers *et al.*, 2000; De Bakker *et al.*, 2016]. However, it can also be observed on the Wadden Sea side (P7–P8 and P9–P10, indicated by positive growth rates between 0.05 and \sim 0.5 Hz). On the other hand, dissipation of infragravity energy was strongest at P2–P3 and was noticeable until \sim P6–P7. Generally, dissipation was stronger across all frequencies for shallow water depths compared to deeper water depths (with the exception of P6–P7), highlighting the importance of inundation depths for energy dissipation. Note that for frequencies \sim >0.5 Hz during the shallow flooding the positive growth onshore of the crest was probably caused by wind forcing. On the other hand, the observed growth at P1–P2 at higher (>0.5 Hz) frequencies could have been caused by nonlinear energy transfers from the spectral peak to higher frequencies [Herbers *et al.*, 2000; De Bakker *et al.*, 2016].

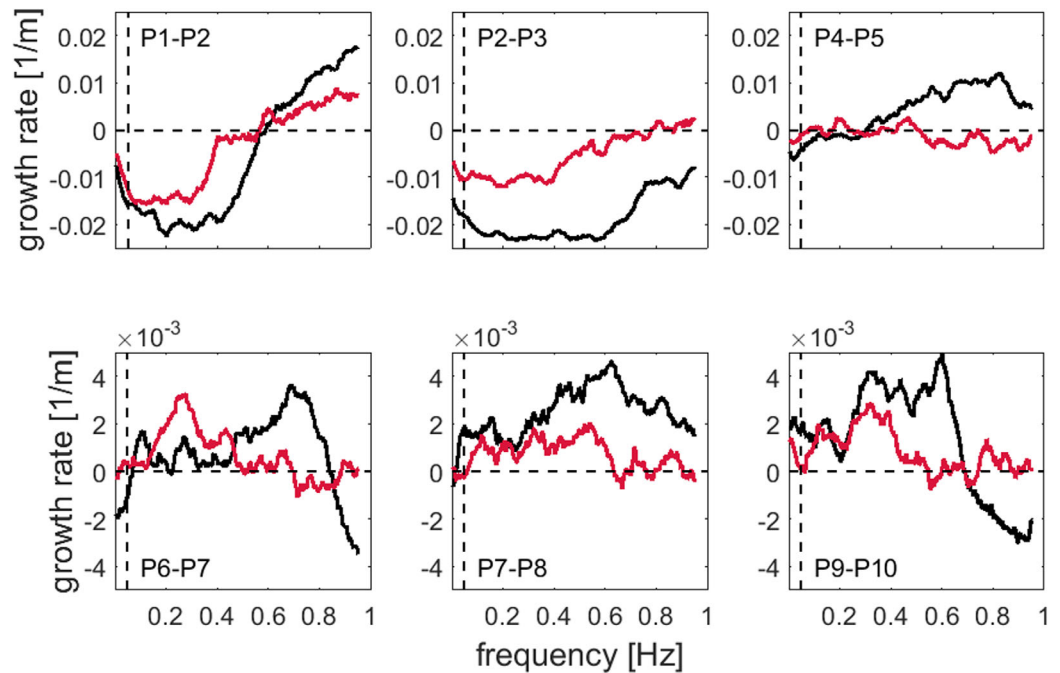


Figure 8. Growth rates are compared for the shallow (black curves) and the deep flooding (red curves) at various locations between the stand-alone pressure sensors from the North Sea side (upper left plot) to the Wadden Sea side (lower right plot). The vertical dashed line shows the cut-off between infragravity (0.005–0.05 Hz) and high-frequency waves. Note the different vertical scales.

To isolate the main dissipation mechanisms, dissipation by wave breaking and by bottom friction was investigated (Figure 9). The breaker coefficient B (equation (7)) was set to 1.5 for the shallow flooding for infragravity and high-frequency waves, while for the deep flooding B was set to 1.8 for infragravity and to 1.0 for high-frequency waves, respectively. B was tuned so that breaking is close to zero at the center of the instrument transect. Wave breaking was the dominant dissipation mechanism (see equation (8) for dissipation by bottom friction) for high-frequency waves before the crest (located at ~ 300 m) and for infragravity waves

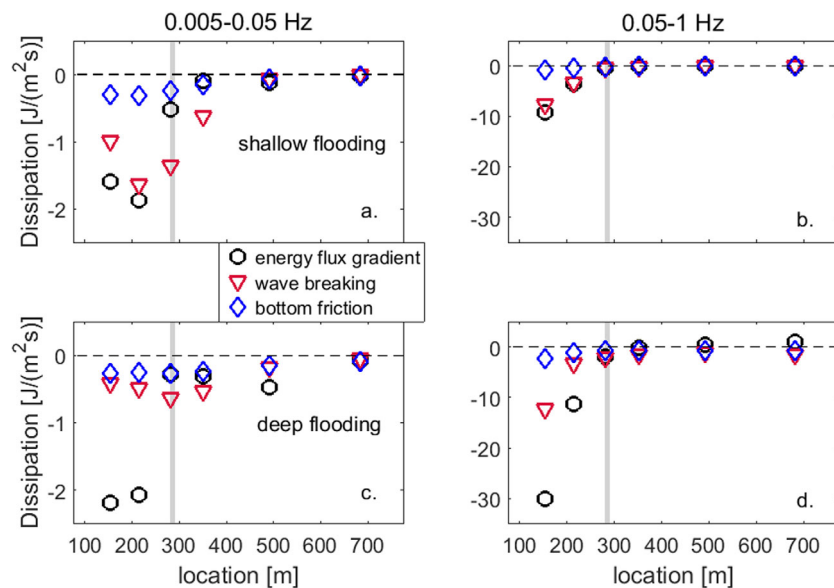


Figure 9. Comparison of energy flux gradients (black circles) and dissipation due to wave breaking (red triangles) and bottom friction (blue diamonds) at the center for (a and b) the shallow flooding and (c and d) the deep flooding for (a and c) low-frequencies and (b and d) high-frequencies. The North Sea is to the left and the Wadden Sea (back-barrier basin) is to the right. The vertical gray line indicates the location of the crest.

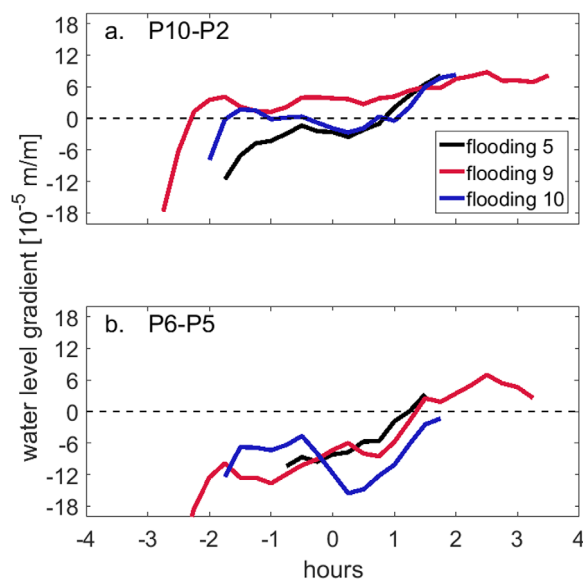


Figure 10. (a) Water-level gradients between the North Sea (P2) side and at the Wadden Sea (P10) side compared to (b) water-level gradients between P5 and P6. Positive values indicate higher water levels at the onshore instrument (the instrument closer to the Wadden Sea side). Negative values indicate higher water levels at the offshore instrument (closer to the North Sea side). The time on the x axis is set relative to high tide (0 h).

On occasions (e.g., floodings 9 and 10) water levels were higher in the Wadden Sea even before high tide (positive values in Figure 10a). However, this was only partially reflected in the local water-level gradients between P5 and P6 where the water-level gradient continued to be directed toward the Wadden Sea (negative values in Figure 10b). This suggests that the wave setup around P5, which was induced by wave breaking, prevented locally a reversal of the water-level gradient.

During times when the water-level gradients around the center ADV reversed toward the North Sea (positive values in Figure 11a), the measured cross-shore currents reversed, too, (Figure 11b) with the exception of the shallow flooding (see section 5.3). However, while depth-averaged onshore velocities reached 0.8 m/s at the center ADV during the deep flooding and 0.2–0.4 m/s during other events, seaward directed flows did not exceed 0.2 m/s and were of much shorter duration. For the Wadden Sea ADV, flow direction reversals were less distinct and pressure gradients and currents (Figures 11c and 11d) were weaker. Here, the onshore directed currents did not exceed 0.2 m/s with the exception of the deep flooding (max \sim 0.5 m/s) and flooding 10 (max \sim 0.35 m/s). Additionally, currents frequently did not reverse even though the local pressure gradient was (briefly) directed offshore (see flooding 5, 8, 9, and 10). In fact, the flow at the Wadden Sea side appears to be closer correlated with the flow measured by the center ADV than with the local water-level gradient (the correlation factors vary between 0.77 and 0.98 for the correlation between the flow measured by the center ADV and the Wadden Sea ADV for all floodings). Variations in water levels at the Wadden Sea side might also have been caused by the influence of a channel located \sim 1 km south of the field site (for a discussion on the limitations of a 1-D—cross-shore, see evaluation see section 5.1). Due to the instrument deployment at different heights of the island, it is difficult to say with certainty if the flooding occurred first from the North Sea or from the Wadden Sea (or from both sides at once). However, the seaward direction of the cross-shore currents at the start of floodings at the Wadden Sea indicates for at least three occasions (negative values in Figure 11d) that the flooding at the Wadden Sea side occurred from the back-barrier basin.

4.3. Momentum Balance

The evaluation of the momentum balance (equation (11)) suggests that during the shallow flooding, at high tide, the onshore-directed (positive) wave force (due to the radiation stress) and the offshore-directed (negative) pressure force (caused by the water-level gradient) roughly balanced offshore off the crest

until \sim P5 (Figure 9). From P7 to the Wadden Sea, dissipation values were too low to determine the dominant dissipation mechanism with certainty and are not shown. Although processes were not captured well at all locations (e.g., the calculated dissipation for the deep flooding was too high at locations after the crest and too low before the crest compared to the energy flux gradient, see also section 5.1), the importance of infragravity wave breaking becomes apparent. This is consistent with earlier results from laboratory studies [Van Dongeren et al., 2007], modeling studies [De Bakker et al., 2016], and shoreline observations [De Bakker et al., 2014].

4.2. Water Level and Current Observations

Observations show that water levels were frequently higher in the Wadden Sea compared to the North Sea (positive values in Figure 10a). This trend was generally observed after high tide and caused the otherwise onshore directed large scale (North Sea-Wadden Sea) water-level gradients (for a definition see section 3.1) to be seaward directed (Figure 10b).

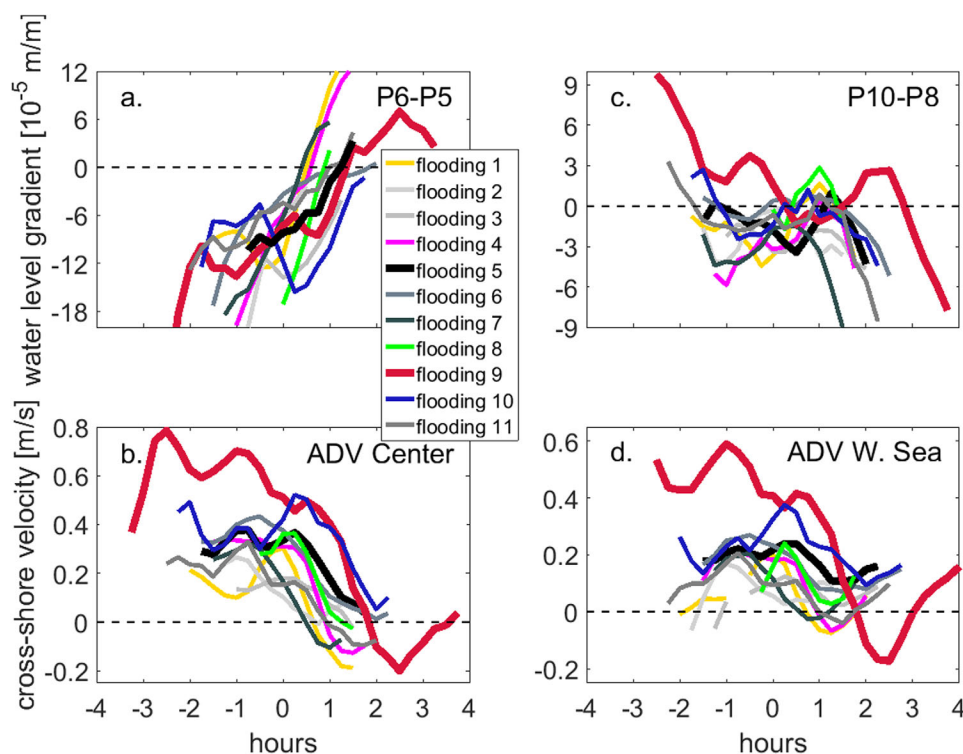


Figure 11. (a) Comparison of water-level gradients between P6 and P5 and (b) currents measured by the center ADV and (c and d) the same comparison for the Wadden Sea between P10 and P8. Positive water-level gradients indicate higher water levels toward the Wadden Sea while negative values indicate higher water levels toward the North Sea. Positive cross-shore currents are directed toward the Wadden Sea. Note that vertical scales are different for the center and the Wadden Sea. The time on the x axis is set relative to high tide (0 h).

(Figure 12a), suggesting that the offshore directed pressure gradient was induced by the breaking waves in the surfzone. Landward of the crest, the pressure gradient was onshore-directed and approximately balanced by bottom friction, suggesting that the onshore flow after the crest was mainly driven by the pressure gradient. This is supported by a comparison of the mean depth-averaged cross-shore velocities measured by the center ADV with velocities calculated (see section 3.3) from the momentum balance (Figure 13a). Contributing to the forcing of the flow during the shallow flooding was the wind (15 m/s from 307° North) which increased onshore flow velocities by about 0.1 m/s (Figure 13a). Even though the wave forcing onshore of the crest was small compared to other forces, omitting the wave force in the calculation of the mean cross-shore velocity u leads to slightly smaller velocities for the onshore flow during the shallow flooding (Figure 13a). The wave forcing was dominated by infragravity wave dissipation (Figure 14a), while the forcing by high-frequency waves was close to zero at the center. At the Wadden Sea side, on the other hand, wave forcing was dominated by high-frequencies while the infragravity wave forcing was close to zero. While currents were not steady over the 1 h at high tide considered here, the acceleration of the flow was small (about two magnitudes smaller than the pressure force), and cross-shore advection is about one magnitude smaller than the pressure force.

During the deep flooding (Figure 12b) at high tide, the pressure gradient fluctuated between offshore and onshore directed offshore of the crest. These fluctuations were probably caused by the more energetic conditions and the deeper water depths, allowing for wave breaking around the crest (Figure 9). The pressure gradient landward of the center frame, at ~500 m, was onshore directed, because the highest water level due to wave setup during the deep flooding was located around the center frame (~450 m). Further toward the Wadden Sea, however, it was offshore directed (with the exception of the location closest to the Wadden Sea), caused by the higher water levels in the back-barrier basin (Figure 10a). Nevertheless, the cross-shore velocities were onshore directed at the center ADV as well as at the Wadden Sea ADV during high tide (Figures 11b and 11d), causing the bottom friction to be negative. Obviously, during the deep flooding the forcing did not balance in most locations. A comparison between measured and calculated cross-shore

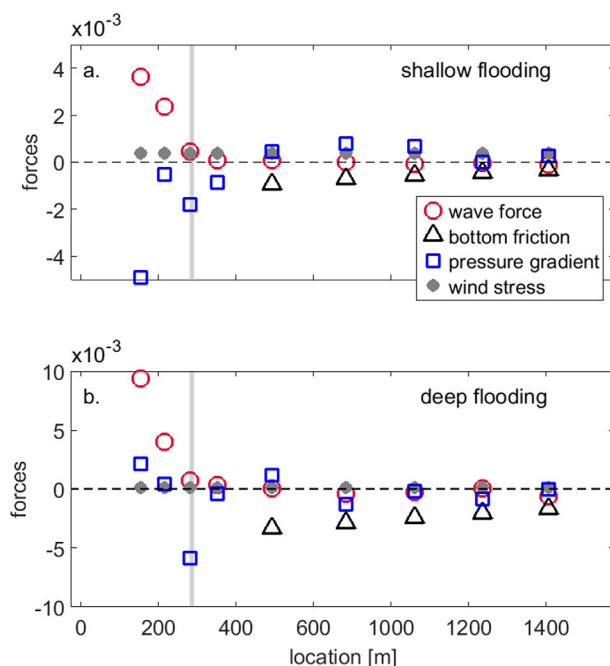


Figure 12. Wave force, bottom friction, pressure gradient, and wind stress at half-way locations between adjacent pressure sensors during (a) the shallow and (b) the deep flooding at high tide. The North Sea is to the left and the Wadden Sea is to the right. The vertical gray line indicates the location of the crest.

in the absence of waves from the Wadden Sea, wave forcing would have had a bigger impact, effectively increasing mean flow velocities. Wind forcing during the deep flooding was small due to the alongshore wind direction (wind speeds of 19 m/s from 260° North) and had only a minor impact (Figure 13b). The pressure force was certainly the most important driver of the flow after the crest during the shallow flooding, while during the deep flooding the mean cross-shore velocities might have been strongly enhanced by surfzone processes.

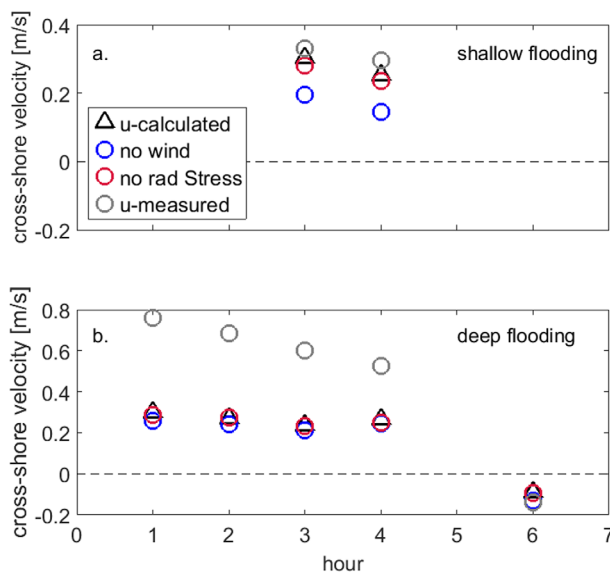


Figure 13. Velocities calculated from the momentum balance are compared to calculations without wind forcing (blue circles) and without wave forcing (red circles) for (a) the shallow and (b) the deep flooding. Shown are also the cross-shore currents measured by the center ADV (gray circles). Time on the x axis is 3 h before and after high tide.

velocities (again at the center ADV) shows (Figure 13b) that the onshore directed flow can only partly be explained by local forcing (the pressure gradient). The underestimation of the calculated velocity suggests that either the local pressure gradient is underestimated, or the mean flow is at least partly driven by wave breaking on the slope before the crest or even further offshore [Symonds *et al.*, 1995]. Additionally, during the deep flooding the magnitude of the alongshore current exceeded the magnitude of the cross-shore current which could have affected the balance (see section 5.1). During the deep flooding, the onshore directed (positive) low-frequency (0.005–0.05 Hz) wave forcing was equal in magnitude to the offshore directed (negative) high-frequency (0.05–1 Hz) wave forcing. Since offshore and onshore wave forcing are almost equal, omitting it in the cross-shore velocity calculation has no effect on the total velocity (Figure 14b), because u is calculated for the range 0.005–1 Hz. This, however, suggests that in the

5. Discussion

5.1. Cross-Shore Evaluation of Wave and Current Processes

The observed wave and current processes during the inundation of the field site were variable in time and space. For instance, waves entered the field area from the North Sea and the Wadden Sea. Further, current directions were onshore directed before high tide, but occasionally reversed direction after high tide. We used a 1-D cross-shore approach to evaluate these processes, since the alongshore variations of the profile were assumed to be negligible in the vicinity of the instrument transect. However, the field site was bordered by a tidal inlet ~2 km to the east and another channel ~1 km to the South, so that the assumption of alongshore uniform water levels might not hold. Further, the measured current directions often had

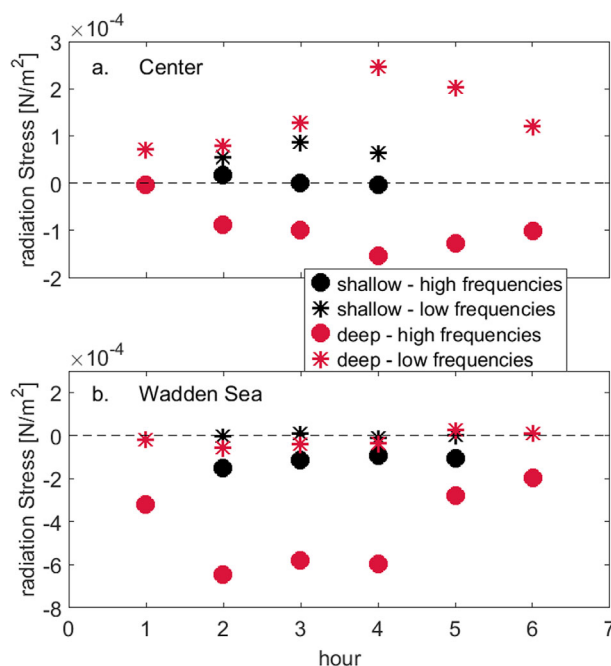


Figure 14. Low-frequency and high-frequency radiation stresses at the center and the Wadden Sea for the shallow and the deep flooding. Time on the x axis is 3 h before and after high tide.

cross-shore advection, rather small. Further, nonlinear wave-wave interactions might have caused a deviation of wave energy from cross-shore [Guza and Feddersen, 2012]. On the other hand, wave directions for the two cases evaluated here were dominantly cross-shore after the crest, allowing for a reasonable estimate of the wave processes. However, a possible explanation for the discrepancy between the energy flux gradient and the combined dissipation of breaking and bottom friction, which can be seen for the first two locations on the North Sea side during the deep flooding (Figures 9c and 9d), could be that the wave direction was not yet cross-shore directed (the offshore wave angle was 312°). This could have potentially lead to an overestimation of the energy flux gradient. Even though the cross-shore evaluation used here might have some limitations, we assume that the main processes during inundation were approximated well.

5.2. Wave Transformation Without Boundaries

Observations of wave transformation during the inundation of the field area showed differences but also some similarities to wave processes on mild sloping (closed) beaches. In the absence of a beach, both infragravity and high-frequency waves were observed to propagate onshore over long stretches of the field site. While wave heights were strongly reduced, the waves did not completely lose all energy (Figures 4–6). This is, of course, different for a closed surfzone-beach-dune system, where wave energy is either dissipated or reflected. Unfortunately, current observations at the North Sea side are missing, and therefore the extent of infragravity wave reflection cannot be established. However, since the field site has a mild slope, it is assumed [Van Dongeren *et al.*, 2007; De Bakker *et al.*, 2014] that reflection is small or nonexistent. Nonetheless, the observation of onshore propagating infragravity waves is in agreement with results by De Bakker *et al.* [2014], and Van Dongeren *et al.* [2007] for mild sloping beaches. Additionally, the dominant dissipation mechanism of infragravity wave energy was found to be wave breaking, which is also consistent with observations on mild sloping beaches [Van Dongeren *et al.*, 2007; De Bakker *et al.*, 2014, 2016].

Our observations during inundation show similarities with observations over a fringing reef by Pomeroy *et al.* [2012], for which infragravity waves were also found to be onshore progressive and increasingly important on the reef flat. Additionally, the authors found infragravity waves to decay over the reef flat, but to lose their energy at a slower rate than the high-frequency waves, something also observed in this study. Van Dongeren *et al.* [2013] used a numerical model to investigate the wave dynamics over the same fringing

a strong alongshore component (not shown). A cross-shore evaluation in these conditions might be an over-simplification of the processes in the area and could explain some of the discrepancies between the observed energy fluxes and the calculated dissipation due to breaking and bottom friction, as well as for the mismatch between calculated and observed velocities for the deep flooding. During the deep flooding, alongshore velocities reached ~ 1 m/s at the center frame and 0.8 m/s at the Wadden Sea which exceeded the maximum measured cross-shore velocities of 0.8 and 0.6 m/s at these locations. In comparison, during the shallow flooding the alongshore velocities reached 0.25 m/s at the center frame and 0.1 m/s at the Wadden Sea compared to cross-shore velocities of 0.4 and 0.25 m/s. Additionally, since we are missing observations for the change in alongshore velocities, we ignored the advective acceleration, $v \frac{dv}{dy}$. This might explain some of the discrepancies, even so we assume that this term will be, like the

reef further. Their results suggest that the dissipation of infragravity waves, and consequently their depth modulation, was primarily due to frictional damping. Our observations showed that dissipation across all frequencies was increased during shallow water depths (Figure 8), which could have been caused either by an increase in bottom friction or by wave breaking. However, the bore-like shape and the higher breaking rates during the shallow flooding suggest that lower water depths enhanced the steepening of infragravity waves and consequently wave breaking. Of course, due to the nature of coral reefs, frictional dissipation will play a much more important role in these environments than over sandy, submerged barrier islands.

5.3. Importance of Back-Barrier Processes

The influence of the back-barrier area on flow processes during overwash and inundation has been reported before. For example, observations of offshore flows, driven by higher water levels in the back-barrier area during ebb tide, were reported by *Sherwood et al.* [2014] for a narrow, low-lying barrier island in Louisiana, USA. Model results based on their observations estimated a mean offshore velocity of 0.20 m/s. For the Netherlands, video-based field observations by *Hoekstra et al.* [2009] in an established washover complex on Schiermonnikoog also suggested that elevated water levels in the back-barrier area (Wadden Sea) drove a flow from the basin side across the island. Model results obtained by *Van Dongeren and Van Ormondt* [2007] were initiated with measured water levels during a storm in 2006. Water levels were higher in the Wadden Sea than in the North Sea for the entire high-tide period, and the model results predicted initial flooding from both sides, as well. A reversal of the mean flow was predicted at a single location (in the washover gap close to the North Sea) ~ 2.5 h after high tide. An explanation for the late reversal of the flow, despite the continuous large-scale (North to Wadden Sea) water-level gradient, could be that wave setup was high due to large offshore wave heights (8.8 m). In the following, we summarize our findings for the processes that are driving the flow during inundation. Typically, the large-scale water-level gradient is onshore directed before high tide (case 1 in Figure 15) due to higher water levels in the North Sea. Additionally, wave setup (generated by the breaking waves) is causing the water level to be highest onshore of the crest. This process creates a pressure force which is offshore directed on the North Sea side and onshore directed at the center and the Wadden Sea. Missing direct measurements, we hypothesize that the flow at the North Sea side will be onshore directed due to momentum and mass conservation. The flow at the center is onshore directed and its magnitude depends on the scale of the driving forces such as pressure gradient, wave force, and bottom friction. On the Wadden Sea side, the flow generally follows the flow at the center (section 4.2), even though the wave force is offshore directed due to the offshore propagating waves from the Wadden Sea. Processes are similar if the wave setup is large, even when water levels are higher in the Wadden Sea (case 2 in Figure 15) than in the North Sea. For example, during flooding 10, the large-scale water-level gradient was offshore directed, while the local water-level gradient was continuously directed onshore (Figure 10). In fact, before high tide the gradient toward the Wadden Sea strengthened (Figure 11a), which was probably caused by an increase in the wave force. This suggests that the local reversal of water-level gradients (and therefore the pressure force) not only depends on the difference between basin and ocean water levels, but also on the offshore wave forcing. If the forcing is strong enough, it can prevent the reversal of the water-level gradient. The water-level gradient, and consequently the flow, reverses when wave setup is small compared to the large-scale water-level gradient (case 3 in Figure 15). For instance, the water level in the Wadden Sea was higher for the entire time during the deep flooding (Figure 10), while the local water-level gradient at the center was still directed toward the Wadden Sea. This only changed about 1 h after high tide, when the water levels in the North Sea dropped further, increasing the difference in large-scale water levels.

In addition, the elevated water levels in the Wadden Sea cannot only cause a reversal of the flow, but it is reasonable to assume that the main effect will be a deceleration of the cross-shore velocities since these decrease with decreasing water-level gradients (Figures 11a and 11b). Furthermore, during the shallow flooding, the flow did not reverse even though the water-level gradient locally reversed about an hour after high tide (Figures 11a and 11b). Calculations of the cross-shore currents suggested that they were enhanced by wind forcing by ~ 0.10 m/s. Together with the small onshore contribution of the wave forcing, it might have prevented the flow reversal.

Processes in the Wadden Sea influenced the current and the wave field in our field area. Of course, the importance of these processes will be regionally different since they depend on local factors such as the size and alignment of the basin, and the tidal inlet(s). The generation of local wind waves in the Wadden

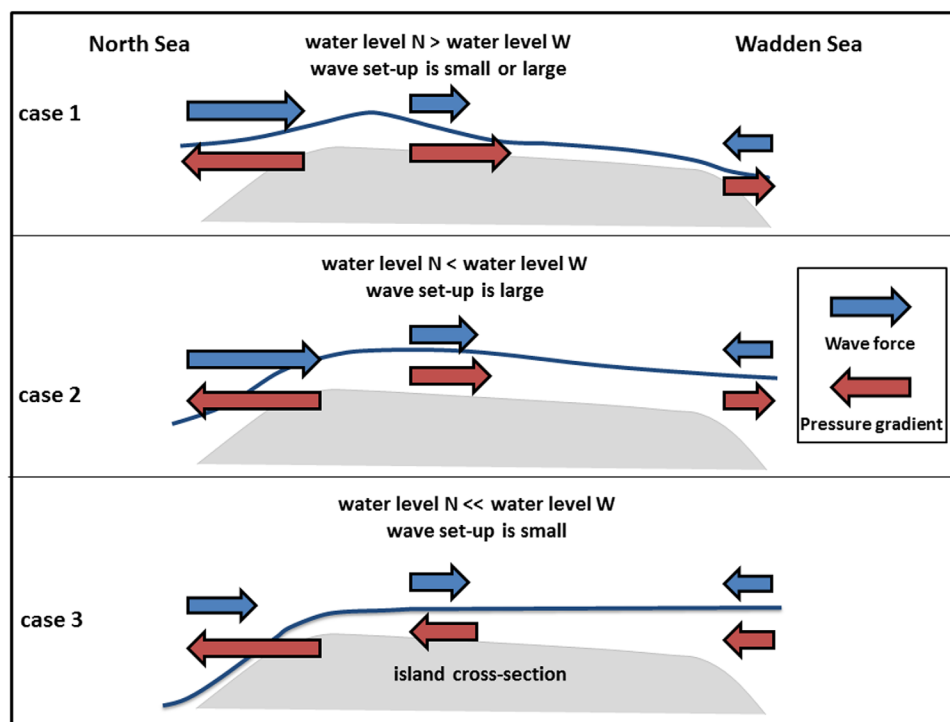


Figure 15. Summary of the main forces that drive the flow, such as pressure gradient (red arrows) and wave force (blue arrows), which depend on water levels (blue curves) in the North (N) and Wadden (W) Sea and the strength of wave setup.

Sea is made possible by the size and alignment of the basin which allows for wave growth during westerly and easterly winds.

6. Conclusions

Observations of water levels, waves, and currents highlight the effect of the back-barrier basin on the hydrodynamics during inundation, as well as the similarities and differences to wave processes on mild sloping beach in a closed surfzone-beach-dune system. High-frequency storm waves and infragravity waves propagated onshore from the North Sea without dissipating all their energy, while waves generated in the Wadden Sea simultaneously propagated offshore. Infragravity waves became equal in magnitude to high-frequency waves onshore of the crest due to the depth-limited breaking of high-frequency waves on the slope. Infragravity wave breaking still continued further onshore on the shallow part of the transect. Generally, infragravity waves were onshore progressive, depth modulated and displayed a bore-like shape in shallow water depths. Wave breaking thus was the dominant dissipation mechanism for high-frequency as well as for infragravity waves, which is in agreement with findings on infragravity wave energy dissipation on mild sloping beaches in a closed-boundary system. Water levels in the back-barrier basin were higher than in the North Sea after high tide and occasionally before (e.g., during the deep flooding), which induced a large-scale offshore directed gradient between Wadden and North Sea. However, due to the wave setup onshore of the crest induced by the wave force, the local gradient at the center was occasionally still onshore directed. On occasions when the large-scale water-level gradient was great enough to overcome the wave setup, the local water-level gradient was also directed offshore and the currents at the center reversed direction with the exception of the shallow flooding when wind forcing was strong. The observation of an offshore flow, forced by elevated water levels in the back-barrier basin is consistent with findings of prior research. In addition to a reversal of the currents, elevated water levels in the back-barrier basin reduced the water-level gradient, effectively slowing the onshore currents. We find that the back-barrier basin is strongly influencing the wave field and current dynamics in our field area.

Acknowledgments

We are greatly indebted to Marcel van Maarseveen, Henk Markies, Chris Roosendaal, and Arjan van Eijk for their excellent technical support. This work was improved by the constructive comments of three reviewers. We would also like to thank Natuurmonumenten for their assistance during the field work. We thank Tim Janssen and Pieter Smit for fruitful discussions and suggestions. This work is supported by the Netherlands Organisation for Scientific Research (NWO) under contract 850.13.051, as well as by Natuurmonumenten, the National Forest Service (Staatsbosbeheer, SBB), and the Wadden Academy. Daan Wesselman is supported by Climate-KIC. The field data can be made available upon request from the first author (A.C.Engelstad@uu.nl).

References

- Christiansen, C., T. Aagaard, J. Bartholdy, M. Christiansen, J. Nielsen, N. Nielsen, J. B. Pedersen, and N. Vinther (2004), Total sediment budget of a transgressive barrier-spit, Skallingen, SW Denmark: A review, *Geogr. Tidsskr. Danish J. Geogr.*, *104*(1), 107–126, doi:10.1080/00167223.2004.10649508.
- De Bakker, A. T. M., M. F. S. Tissier, and B. G. Ruessink (2014), Shoreline dissipation of infragravity waves, *Cont. Shelf Res.*, *72*, 73–82, doi:10.1016/j.csr.2013.11.013.
- De Bakker, A. T. M., M. F. S. Tissier, and B. G. Ruessink (2016), Beach steepness effects on nonlinear infragravity-wave interactions: A numerical study, *J. Geophys. Res. Oceans*, *121*, 554–570, doi:10.1002/2015JC011268.
- Donnelly, C., N. Kraus, and M. Larson (2006), State of knowledge on measurement and modeling of coastal overwash, *J. Coastal Res.*, *22*, 965–991, doi:10.2112/04-0431.1.
- Edge, B. L., Y. H. Park, and M. Overton (2007), Experimental study of overwash, in *Proceedings Coastal Sediments*, vol. 7, pp. 2074–2083, Am. Soc. of Civ. Eng., Reston, Va., doi:10.1061/40926(239)163.
- Elgar, S., B. Raubenheimer, and R. T. Guza (2005), Quality control of acoustic Doppler velocimeter data in the surfzone, *Meas. Sci. Technol.*, *16*(10), 1889, doi:10.1088/0957-0233/16/10/002.
- Fisher, J. S., S. P. Leatherman, and F. C. Perry (1974), Overwash processes on Assateague Island, in *Proceedings of 14th Conference on Coastal Engineering*, pp. 1194–1211, ASCE, Copenhagen, Denmark, doi:10.1061/9780872621138.073.
- FitzGerald, D. M., and E. Pendleton (2002), Inlet formation and evolution of the sediment bypassing system: New Inlet, Cape Cod, Massachusetts, *J. Coastal Res.*, *36*, 290–299, doi:10.1029/ce044p0158.
- Grunnet, N. M., D.-J. R. Walstra, and B. G. Ruessink (2004), Process-based modelling of a shoreface nourishment, *Coastal Eng.*, *51*(7), 581–607, doi:10.1016/j.coastaleng.2004.07.016.
- Guza, R. T., and F. Feddersen (2012), Effect of wave frequency and directional spread on shoreline runup, *Geophys. Res. Lett.*, *39*, L11607, doi:10.1029/2012GL051959.
- Guza, R. T., and E. B. Thornton (1985), Observations of surf beat, *J. Geophys. Res.*, *90*, 3161–3172, doi:10.1029/JC090iC02p03161.
- Herbers, T. H. C., S. Elgar, R. T. Guza, and W. C. O'Reilly (1995), Infragravity-frequency (0.005–0.05 Hz) motions on the shelf. Part II: Free waves, *J. Phys. Oceanogr.*, *25*(6), 1063–1079, doi:10.1175/1520-0485(1995)025<1063:IFHMOT>2.0.CO;2.
- Herbers, T. H. C., N. R. Russnogle, and S. Elgar (2000), Spectral energy balance of breaking waves within the surf zone, *J. Phys. Oceanogr.*, *30*(11), 2723–2737, doi:10.1175/1520-0485(2000)030<2723:sebobw>2.0.co;2.
- Hoekstra, P., M. ten Haaf, P. Buijs, A. Oost, R. Klein Breteler, K. van der Giessen, and M. van der Vegt (2009), Washover development on mixed-energy, mesotidal barrier island systems, in *Coastal Dynamics*, edited by Masaru Mizuguchi and Shinji Sato, vol. 83, pp. 25–32, World Sci., Singapore.
- Holland, K. T., R. A. Holman, and A. H. Sallenger (1991), Estimation of overwash bore velocities using video techniques, in *Coastal Sediments*, edited by N. C. Kraus, K. J. Gingerich, D. L. Kriebel, and American Society of Civil Engineers, Committee on Coastal Engineering pp. 489–497, University of Mich., Ann Arbor, doi:10.5670/oceanog.1993.02.
- Janssen, T. T., J. A. Battjes, and A. R. van Dongeren (2003), Long waves induced by short-wave groups over a sloping bottom, *J. Geophys. Res.*, *108*(C8), 3252, doi:10.1029/2002JC001515.
- Leatherman, S. P. (1976), Barrier island dynamics: Overwash processes and Eolian transport, *Coastal Eng. Proc.*, *1*(15), 1958–1974, doi:10.1061/9780872620834.114.
- Loeffler, M. A. M., C. C. de Leeuw, M. E. ten Haaf, S. K. Verbeek, A. P. Oost, A. P. Grootjans, E. J. Lammerts, and R. M. K. Haring (2011), *Back to Basics*, Het Tij Geleerd (Waddervereniging, SSB, Natuurmonumenten, Rijkswaterstaat, It Fryske Gea) ru-Groningen, Radboud Universiteit Nijmegen, RU-Utrecht ed., 44 pp., ERA.
- Longuet-Higgins, M. S., and R. W. Stewart (1964), Radiation stresses in water waves: A physical discussion, with applications, *Deep Sea Res. Oceanogr. Abstr.*, *11*(4), pp. 529–562, doi:10.1016/0011-7471(64)90001-4.
- Matias, A., Ó. Ferreira, A. Vila-Concejo, T. Garcia, and J. A. Dias (2008), Classification of washover dynamics in barrier islands, *Geomorphology*, *97*(3), 655–674, doi:10.1016/j.geomorph.2007.09.010.
- Matias, A., Ó. Ferreira, A. Vila-Concejo, B. Morris, and J. A. Dias (2010), Short-term morphodynamics of non-storm overwash, *Mar. Geol.*, *274*(1), 69–84, doi:10.1016/j.margeo.2010.03.006.
- Matias, A., G. Masselink, A. Kroon, C. E. Blenkinsopp, and I. L. Turner (2013), Overwash experiment on a sandy barrier, *J. Coastal Res.*, *1*(65), 778, doi:10.2112/si65-132.1.
- McCall, R. T., J. S. M. Van Thiel De Vries, N. G. Plant, A. R. Van Dongeren, J. A. Roelvink, D. M. Thompson, and A. J. H. M. Reniers (2010), Two-dimensional time dependent hurricane overwash and erosion modeling at Santa Rosa Island, *Coastal Eng.*, *57*(7), 668–683, doi:10.1016/j.coastaleng.2010.02.006.
- McCall, R. T., N. Plant, and J. Van Thiel de Vries (2011), The effect of longshore topographic variation on overwash modelling, *Coastal Eng. Proc.*, *1*(32), 36, doi:10.9753/icce.v32.sediment.36.
- Mori, N., T. Suzuki, and S. Kakuno (2007), Noise of acoustic Doppler velocimeter data in bubbly flows, *J. Eng. Mech.*, *133*(1), 122–125, doi:10.1061/(ASCE)0733-9399(2007)133:1(122).
- Morton, R. A., and A. H. Sallenger Jr. (2003), Morphological impacts of extreme storms on sandy beaches and barriers, *J. Coastal Res.*, *19*, 560–573.
- Nielsen, N., and J. Nielsen (2006), Development of a washover fan on a transgressive barrier, Skallingen, Denmark, *J. Coastal Res.*, *39*, 107–111.
- Oost, A. P., et al. (2012), Barrier island management: Lessons from the past and directions for the future, *Ocean Coastal Manage.*, *68*, 18–38, doi:10.1016/j.ocecoaman.2012.07.010.
- Pomeroy, A., R. Lowe, G. Symonds, A. Van Dongeren, and C. Moore (2012), The dynamics of infragravity wave transformation over a fringing reef, *J. Geophys. Res.*, *117*, C11022, doi:10.1029/2012JC008310.
- Raubenheimer, B., S. Elgar, and R. T. Guza (1998), Estimating wave heights from pressure measured in sand bed, *J. Waterway Port Coastal Ocean Eng.*, *124*(3), 151–154, doi:10.1061/(ASCE)0733-950X(1998)124:3(151).
- Ruessink, B. G., M. G. Kleinhans, and P. G. L. den Beukel (1998), Observations of swash under highly dissipative conditions, *J. Geophys. Res.*, *103*, 3111–3118, doi:10.1029/97JC02791.
- Ruessink, B. G., J. R. Miles, F. Feddersen, R. T. Guza, and S. Elgar (2001), Modeling the alongshore current on barred beaches, *J. Geophys. Res.*, *106*, 22,451–22,463, doi:10.1029/2000JC000766.
- Ruessink, B. G., D. J. R. Walstra, and H. N. Southgate (2003), Calibration and verification of a parametric wave model on barred beaches, *Coastal Eng.*, *48*(3), 139–149, doi:10.1016/S0378-3839(03)00023-1.

- Safak, I., J. C. Warner, and J. H. List (2016), Barrier island breach evolution: Alongshore transport and bay-ocean pressure gradient interactions, *J. Geophys. Res. Oceans*, *121*, 8720–8730, doi:10.1002/2016JC012029.
- Sallenger Jr., A. H. (2000), Storm impact scale for barrier islands, *J. Coastal Res.*, 890–895, doi:10.1306/44b4ba04-170a-11d7-8645000102c1865d.
- Sherwood, C. R., J. W. Long, P. J. Dickhudt, P. S. Dalyander, D. M. Thompson, and N. G. Plant (2014), Inundation of a barrier island (Chandeleur Islands, Louisiana, USA) during a hurricane: Observed water-level gradients and modeled seaward sand transport, *J. Geophys. Res. Earth Surf.*, *119*, 1498–1515, doi:10.1002/2013JF003069.
- Symonds, G., K. P. Black, and I. R. Young (1995), Wave-driven flow over shallow reefs, *J. Geophys. Res.*, *100*, 2639, doi:10.1029/94JC02736.
- Thornton, E. B., and R. T. Guza (1983), Transformation of wave height distribution, *J. Geophys. Res.*, *88*, 5925–5938, doi:10.1029/jc088ic10p05925.
- Van der Vegt, M., and P. Hoekstra (2012), Morphodynamics of a storm-dominated, shallow tidal inlet: The Slufter, the Netherlands, *Neth. J. Geosci.*, *91*(3), 325–339, doi:10.1017/s0016774600000470.
- Van Dongeren, A., and M. Van Ormondt (2007), Hydrodynamic aspects of overwash, *Framework: H&I Zeereep (Report in Dutch)*, report Z, 4412, 33, WL Delft Hydraulics.
- Van Dongeren, A., J. Battjes, T. Janssen, J. Van Noorloos, K. Steenhauer, G. Steenbergen, and A. J. H. M. Reniers (2007), Shoaling and shoreline dissipation of low-frequency waves, *J. Geophys. Res.*, *112*, C02011, doi:10.1029/2006JC003701.
- Van Dongeren, A., R. Lowe, A. Pomeroy, D. M. Trang, D. Roelvink, G. Symonds, and R. Ranasinghe (2013), Numerical modeling of low-frequency wave dynamics over a fringing coral reef, *Coastal Eng.*, *73*, 178–190, doi:10.1016/j.coastaleng.2012.11.004.
- Wamdi Group (1988), The WAM model—a third generation ocean wave prediction model, *J. Phys. Oceanogr.*, *18*(12), 1775–1810, doi:10.1175/1520-0485(1988)018<1775:twmtgo>2.0.co;2.
- Wu, J. (1982), Wind-stress coefficients over sea surface from breeze to hurricane, *J. Geophys. Res.*, *87*, 9704–9706, doi:10.1029/jc087ic12p09704.
- Zijlema, M., G. Stelling, and P. Smit (2011), SWASH: An operational public domain code for simulating wave fields and rapidly varied flows in coastal waters, *Coastal Eng.*, *58*(10), 992–1012, doi:10.1016/j.coastaleng.2011.05.015.